International Journal of Physical Sciences Vol. 2 (6), pp. 149-158, June, 2007
Available online at http://www.academicjournals.org/IJPS
ISSN 1992 - 1950 © 2007 Academic Journals

Full Length Research Paper

Image enhancement using second generation wavelet super resolution

M. El-Sayed Wahed

Department of Mathematics, Faculty of Science, Zagazig University, Zagazig, Egypt. E-mail: mewahed@yahoo.com

Accepted 15 May, 2007

Second generation wavelet based super resolution algorithms developed in this research are presented in this paper. Generalization of the Second generation wavelet super resolution (SGWSR) algorithm to handle arbitrarily irregular 2-D grids as opposed to the semi-regular grids handled in the previous algorithm is introduced. A consequence is the ability to incorporate the projective camera motion model into the framework. Simultaneous noise filtering with super resolution is achieves. The generalization to the arbitrary 2-D version is subsequently described. Simulation results which demonstrate the improved performance of the developed super resolution algorithms in comparison to other approaches are also presented.

Key words: Super resolution, second generation wavelets, blind deconvolution, optimal thresholding, blur support determination.

INTRODUCTION

The field of super resolution has seen a tremendous growth in interest over the past decade. High resolution images are crucial in several applications including medical imaging and diagnosis, military surveillance, satellite and astronomical imaging, and remote sensing. Constraints due to factors such as technology, cost, size, weight, and quality prevent the use of sensors with the desired resolution in image capture devices and conesquently, necessitate the design of superresolution algorithms to achieve the desired image resolution. The process of image registration with respect to a reference frame results in a grid with irregularly spaced sampling points. Hence, the superresolution algorithm needs to handle irregular sampling (Bose et al., 2004).

Unfortunately, most algorithms employ some means of approximating the irregularly sampled grid with a regularly sampled one. This induces some error in the process of superresolution which is reflected in the output image quality (Bose et al., 2004).

It is then reasonable to expect an improvement in performance from a super-resolution algorithm which is capable of handling the irregular samples without approximations.

The ability of second generation wavelets (Zayed et al., 2006) to adapt to irregular sampling intervals rendered them an ideal starting point for this research. The additional property of handling arbitrary boundaries eliminates the need to assume and impose assumptions like the zero, periodic and Neumann boundary conditions and enhances the probability of obtaining better results from a superresolution algorithm based on second gene-ration wavelets. The possibility of achieving simultaneous noise reduction by the use of wavelet coefficient thresholding provided an added incentive to delve deeper in this direction.

Consequently, one of the main objectives of this research was the development of algorithms based on second generation wavelets for superresolution with the capability of simultaneous noise reduction.

Blind deconvolution is an inverse problem with insufficient data. It is therefore desirable to exploit the extra information available in multiple frames in the superresolution problem. Among the many techniques available for blind deconvolution, few extend directly and easily to the multi-frame case. One of the best algorithms (in terms of performance and complexity) was the asymmetric iterative blind deconvolution (IBD) algorithm proposed by Biggs and Andrews (Vanraes et al., 2002; Starck et al., 2002). But this algorithm relies on the assumption of a priori knowledge, or alternatively, trial-and-error estimation, of the support of the blurring function and the asymmetry factor for optimal performance. Other single fra-

me approaches to blind deconvolution like the regularization based approach of Waheed and Mohammed (2006) include modules for estimating the support of the blurring function or PSF.

The efficacy of the proposed enhancements is evidenced by the presented simulation results. The organization of the rest of the paper is as follows:

Section 2. Describe Pre-Processing; Section 3. Given Simultaneous Noise Filtering; Section. 4. SGW Superresolution on Arbitrarily Irregular Grids; Section 5. Introducing the Refinement Relations; Section 6. Describes Prediction and Update; Section 7. Given Algorithm; Section 8. Simulation Results. Finally, some conclusions are given in sec. 9.

PRE-PROCESSING

The quality of the super resolved HR image may be adversely affected due to the presence of one or a few input LR frames which have been either severely blurred or degraded by additive noise. In comparison to the remaining majority of the input LR frames, these severely corrupted frames do not contribute to the improvement in image quality that is sought by the superresolution algorithm. On the contrary, they degrade the quality of the generated HR image. Rejecting such frames from being used as inputs constitutes a simple pre-processing step to the superresolution algorithm which avoids unnecessary loss of reconstructed HR image quality. The identification of the 'bad frames' based on the frame variances was proposed in (Lertrattanapanich and Bose, 2002) on an intuitive basis. The approach is also employed in this research and a simple mathematical justification is also provided. Since LR frames contain a significantly large common region of interest, it can be assumed that the variances of a set of LR frames, $\{f_l\}$, should be reasonably close to one another. If an LR frame is severely corrupted by additive noise, its variance will be much higher than those of other acceptable LR frames. In contrast, if an LR frame is severely blurred, its variance will be much lower than that of other acceptable LR frames.

Simultaneous noise filtering

Image acquisition is usually subject to the degrading effect of noise corruption. Thus, the LR inputs to the superresolution algorithm are typically noisy. Most of the existing superresolution algorithms counter the input noise by including a separate denoising module that processes the generated HR image. Examples of techniques for denoising images range from simple averaging to more sophisticated methods documented in (Moayeri and Konstantinides, 1996). Though some of these techniques are indeed very effective for denoising images, the opposed to the computational complexity of the implementation is considerably high.

Since, in general, superresolution algorithms themselves are computation intensive, a denoising technique which can be incorporated with minimal increase in computational complexity while providing reasonably good performance is desirable. The superresolution algorithms developed in this research (which are subsequently presented in Sections 4.3 and 4.4) involve the compu-tation of second generation wavelet coefficients. There-fore, the denoising technique based on wavelet coeffi-cient thresholding (Donoho, 1995) is selected since it allows simultaneous noise filtering with superresolution, thereby reducing computation cost significantly in the overall framework. It is important to note that thresholding in the SGW setting is much more challenging than in the FGW case since small coefficients may carry important information which is essential for a stable inverse trans-form (Moayeri and Konstantinides, 1996).

The SGW based HR reconstruction methods simultaneously incorporate noise filtering by hard/soft thresholding of wavelet coefficients defined, respectively, by the following expressions (Donoho, 1995):

$$d_h = \begin{cases} d, & d \phi \xi \\ 0, & -\xi \le d \le \xi \\ -d, & d \pi \xi \end{cases},$$

$$d_s = \begin{cases} d - \xi, & d \phi \xi \\ 0, & -\xi \le d \le \xi \\ -d + \xi, & d \pi \xi \end{cases} \quad (1)$$

Where d represents an SGW coefficient before thresholding and ξ is the threshold. The response curves for the two thresholding schemes are illustrated in Figure 1. The efficacy of this process of thresholding relies on the decorrelating properties of the wavelet transform. Essentially, if the random noise corrupting an image is uncorrelated with the image itself (which is the most common case), the application of a wavelet transform results in the noise being captured mainly in the wavelet coefficients. Soft thresholding yields better results as will be shown in simulations presented subsequently.

SGW superresolution on arbitrarily irregular grids

When camera motions more general and complex than translation (such as affine and projective) are considered, the resulting grid of registered LR samples is not semi-regular. On the contrary, it is two-dimensionally arbitrarily irregular, an example of which is given In Figure 2. Achieving superresolution over such arbitrary grids is more challenging and necessitates generalizations and modifications to the algorithm were first proposed in (Waheed and Mohammed, 2006). The ability to handle arbitrarily irregular grids or sampling lattices results from the use of 2-D prediction and update operators as opposed to the

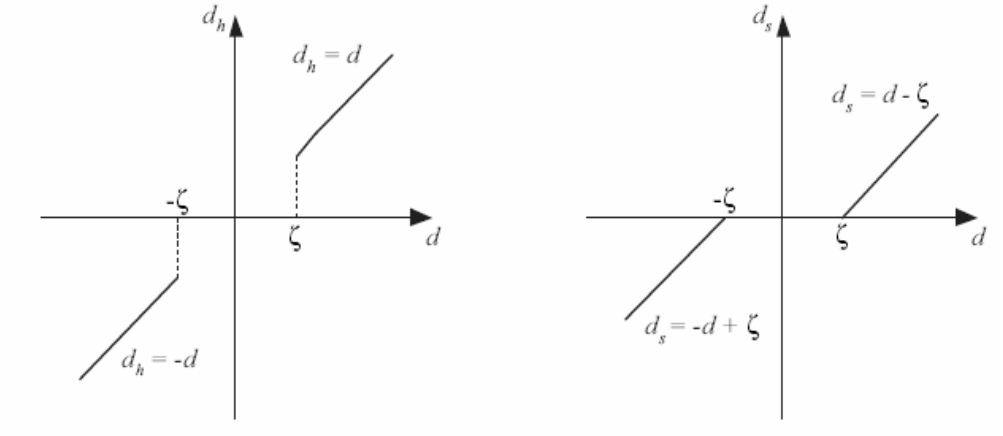

Figure 1. Hard and Soft thresholding.

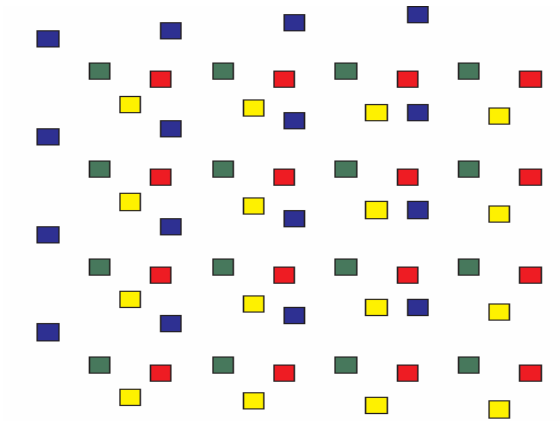

Figure 2a. 2-D arbitrarily irregular grid of registered LR frames

tensor product of 1-D operators.

Refinement relations

Due to the Multi-Resolution Analysis (MRA) structure, there exist refinement coefficients $\{\beta_{j,t,k}\}$ and $\{\gamma_{j,t,l}\}$ at the j^{th} level such that

$$\varphi_{j,k} = \sum_{t \in k_{j+1}} \beta_{j,t,k} \varphi_{j+1,l}$$

$$\psi_{j,l} = \sum_{t \in k_{j+1}} \lambda_{j,t,l} \varphi_{j+1,l} \qquad (2)$$

In matrix notation with $\Phi_j = [\varphi_{j,1} \quad \varphi_{j,2} \ldots]$ and $\Psi_j = [\psi_{j,1} \quad \psi_{j,1} \ldots]$

$$\Phi_j = \Phi_{j+1} \beta_j \quad ; \quad \Psi_j = \Psi_{j+1} \gamma_j \qquad (3)$$

Where β_j and γ_j are matrices whose rows contain coefficients in accordance with Equation (2). Dual scaling functions and wavelets also have similar refinement relations which can be expressed as

$$\bar{\Phi}_j = \bar{\Phi}_{j+1} \bar{\beta}_j \quad ; \quad \bar{\Psi}_j = \bar{\Psi}_{j+1} \bar{\gamma}_j \qquad (4)$$

Where matrices $\bar{\beta}_j$ and $\bar{\gamma}_j$ are formed similar to matrices β_j and γ_j defined above.

Then $$\bar{\beta}^*_j \beta_j = I, \quad ; \quad \bar{\gamma}^*_j \beta_j = 0 \qquad (5)$$

$$\bar{\beta}^*_j \gamma_j = 0, \qquad \bar{\gamma}^*_j \gamma_j = I \qquad (6)$$

Where * represents the Hermitian operator. Thus, for any given s_j, the forward wavelet
Transform or analysis is given by

$$s_{j-1} = \bar{\beta}^*_j s_j \qquad d_{j-1} = \bar{\gamma}^*_j s_j \qquad (7)$$

Pre-multiplying the two expressions in Equation (7) above by β_{j-1} and γ_{j-1} respectively and adding yields the expression for the inverse transform or synthesis as:

$$\beta_{j-1} s_{j-1} + \gamma_{j-1} d_{j-1} = [\beta_{j-1} \bar{\beta}^*_{j-1} + \gamma_{j-1} \bar{\gamma}^*_{j-1}] s_j = I s_j = s_j \qquad (8)$$

For any given operator P_j at the j^{th} level and an initial biorthogonal filter pair $(\overset{(0)}{\beta}_j \overset{(0)}{\gamma}_j)$, $(\overset{-(0)}{\beta}_j \overset{-(0)}{\gamma}_j)$ a new set of biorthogonal filters can be computed using the expressions

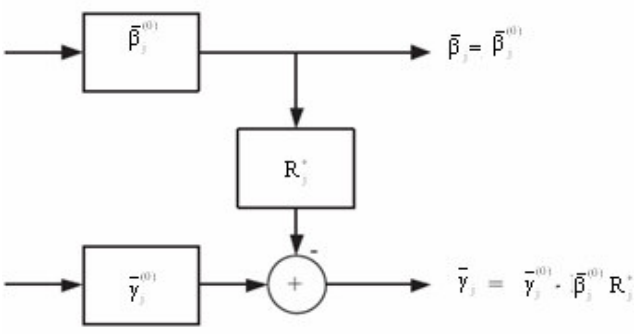

Figure 2b. Prediction step: analysis.

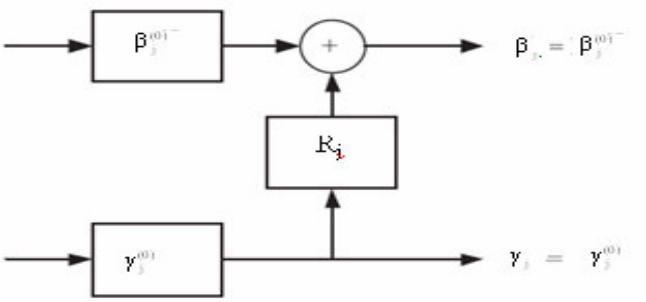

Figure 3. Prediction step: synthesis.

$$\bar{\beta}_j = \bar{\beta}_j^{(0)}, \qquad \bar{\gamma}_j = \bar{\gamma}_j^{(0)} - \bar{\beta}_j^{(0)} P_j^* \qquad (9)$$

$$\beta_j = \beta_j^{(0)} + \gamma_j^{(0)} P_j, \qquad \gamma_j = \gamma_j^{(0)} \qquad (10)$$

The above step is known as the prediction step and is graphically illustrated in Figures 2 and 3. As seen, Equation (9) corresponds to the analysis prediction step whereas.
Equation (9) corresponds to the synthesis prediction step.

Note: It is conventional to use $\bar{\beta}_j$ and $\bar{\gamma}_j$ to represent the analysis filters and β_j and γ_j to represent the synthesis filters.

Interchanging the roles of the primal and the dual MSDs in Equations (9) and (10) above, for any operator Uj ,

$$\bar{\beta}_j = \bar{\beta}_j^{(0)} + \bar{\gamma}_j^{(0)} U_j^*, \qquad \bar{\gamma}_j = \bar{\gamma}_j^{(0)} \qquad (11)$$

$$\beta_j = \beta_j^{(0)}, \qquad \gamma_j = \gamma_j^{(0)} - \beta_j^{(0)} U_j \qquad (12)$$

This is termed as the update step. As before, Equation

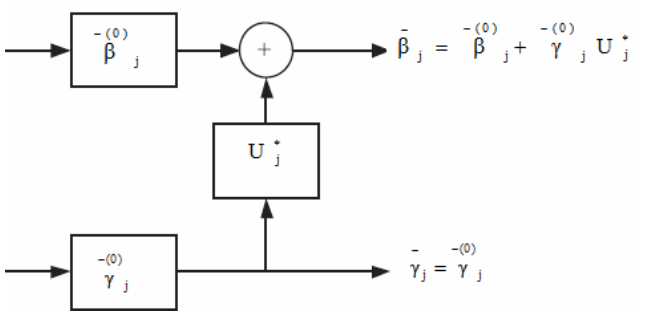

Figure 4. Update step: analysis

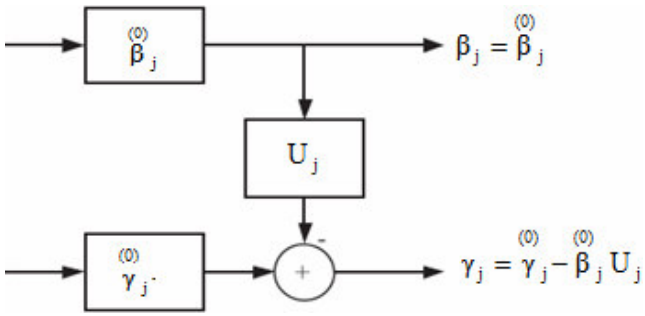

Figure 5. Update step: synthesis

(11) corresponds to the analysis side update step while Equation (12) corresponds to the synthesis side update step. These equations are depicted pictorially in Figures 4 and 5. A point to be noted is that in the analysis side, the update step follows the prediction step and hence the initial filters for the update step are those which have already been processed by the prediction step. The converse occurs in the synthesis side since the prediction step follows the update.

One commonly used choice for the initial trivial biorthogonal filter pair is given by the lazy wavelets transform which involves no computation but which has the formal properties of a wavelet transform. It involves a simple splitting or subsampling of the data into even (approximation) and odd (detail) indexed sets. This corresponds to the choice

$$\bar{\gamma}_j = \bar{\gamma}_j^{(0)} = \{s_{j+1,0}\}, \qquad \beta_j^{(0)} = \bar{\beta}_j^{(0)} = \{N(s_{j+1,0})\} \qquad (13)$$

where $s_{j+1,0}$ is the scaling function coefficient being predicted and $N(s_{j+1,0})$ denotes the neighborhood of $s_{j+1,0}$ (set of points in the vicinity of $s_{j+1,0}$ which satisfy a certain property). Elements belonging to this neighborhood are modified in the update step. Figure 6 illustrates the lifting scheme for this choice of initial filters.

Since there are no restrictions on how the prediction neighborhood is chosen, the definition of the neighborhood can be modified at the boundaries in such a manner

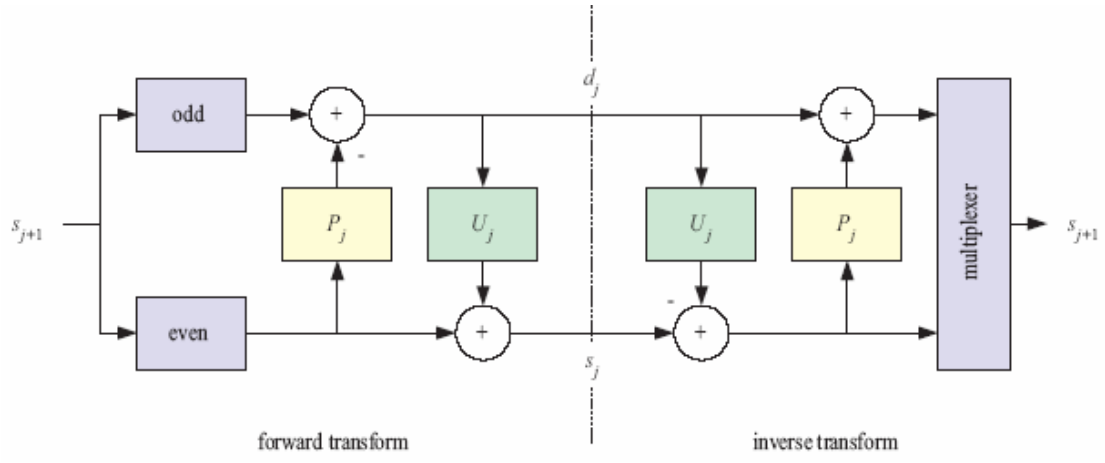

Figure 6. Lifting scheme with the lazy wavelet as the starting step.

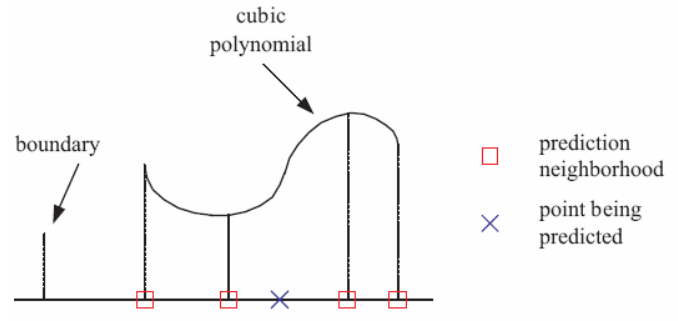

Figure 7. Cubic polynomial prediction: unaffected by the boundary.

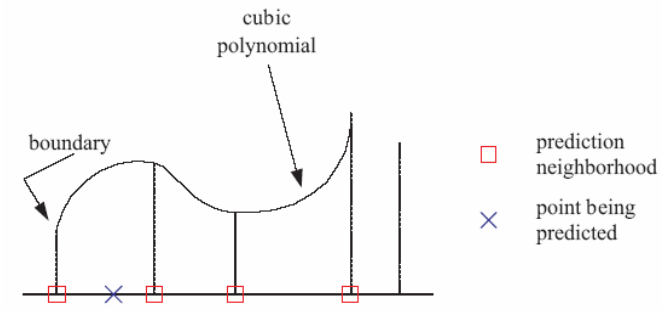

Figure 8. Cubic polynomial prediction: affected by the boundary.

that assumptions in the form of boundary conditions are rendered unnecessary. For example, consider a cubic polynomial predictor. Since a cubic polynomial is uniquely determined by four points, the prediction neighborhood should include four points. Typically, two data points on either side of the point being predicted are used for the prediction, as illustrated in Figure 7. At boundaries however, two points may not be available on either side. In such cases, the prediction neighborhood selection can be modified to use the four nearest data points (for example, a single point on one side and three on the other side) to determine the predictor function, as illustrated in Figure 8. The outlined procedure clearly preserves the cubic reconstruction property even at boundaries and is hence an appropriate choice for handling boundaries without imposing boundary conditions. It should be noted that the neighborhood and the cubic polynomial curve remains the same, though the prediction coefficients will be different, for the prediction of any point between the second and third samples from the left in Figure 8. Further, none of the aspects of the construction using the lifting technique imposes a requirement for uniformly spaced data points. This flexibility in construction using the lifting technique enables SGWs to adapt to general settings like bounded domains and irregular samples. It should be noted that the use of asymmetric prediction neighborhoods at boundaries tends to introduce a bias towards the interior values in the reconstruction (Vanraes et al., 2002). The solution suggested in Vanraes et al. (2002) to overcome this problem is to enforce symmetric prediction neighborhoods at the boundaries by giving up some vanishing moments.

PREDICTION AND UPDATE

From the expression for the forward transform given in Equation (2), the detail or wavelet coefficient that replaces the scaling function coefficient $s_{j+1},0$ can be computed as follows

$$d_{j,0} = \bar{\gamma}^{*}_{j+1} s_{j+1}$$

Using the refinement relation in Equation (3)

$$d_{j,0} = \bar{\gamma}^{(0)*}_{j+1} s_{j+1} - R_{j+1} \bar{\beta}^{(0)*}_{j+1} s_{j+1}$$

For the initial filters given in Equation (5)

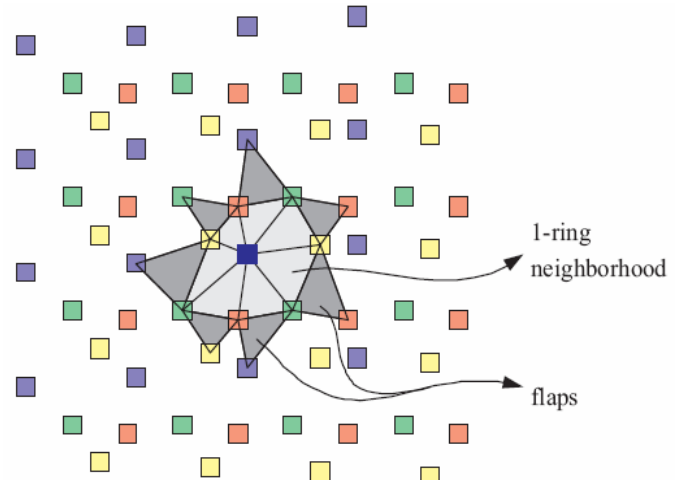

Figure 9. 1-ring neighborhood of a point.

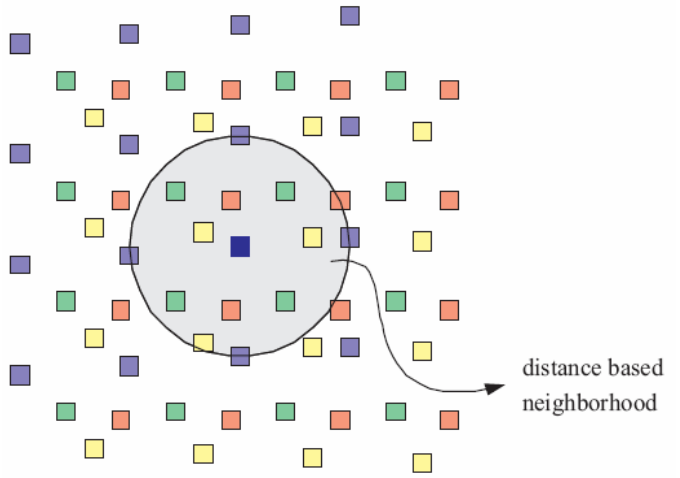

Figure 10. Distance-based neighborhood of point.

$$d_{j,0} = s_{j+1,0} - R_{j+1}[N(s_{j+1,0})] \quad (14)$$

The generic 2-D setting allows the definition of a much larger variety of neighborhoods. Three types of neighborhoods are illustrated in Figures 6, 7 and 8 with the point being predicted shown in bright blue in the center of the grid. The first, illustrated in Figure 6, is the 1-ring neighborhood

Which is defined based on the Delaunay triangulation (Okabe et al., 1992) of the registered irregularly spaced samples. The triangles shown in the figure are Delaunay triangles. The 1-ring neighborhood is thus the set of points whose Delaunay triangles contain the point being predicted. Further discussions in this paper assume a 1-ring prediction neighborhood, though the concepts also apply to other types of neighborhoods. The definition of the 1-ring neighborhood can be easily generalized. A 1-ring neighborhood with flaps is the union of the 1-ring neighborhood and the triangles filled with dark gray in the figure. Further larger neighborhoods such as the 2-ring neighborhood can be similarly defined.

Another type of neighborhood can be defined based on a distance criterion and is shown in Figure 9. The neighborhood consists of all points which lie within a specified Euclidean distance from the point being predicted. The 1-ring and the distance based neighborhoods are generic in the sense that they are determined only by the locations of the samples and not based on the pixel values at the locations. The adaptive neighborhood shown in Figure 10 takes the pixel values also into account and achieves much better edge reconstruction.

As a specific example of a prediction operator, consider a least-squares plane predictor. Consider the prediction of a point $p_0(x_0, y_0)$ and with pixel value z_0. Let $p_k = 1, \ldots, K$, where $K = \frac{(\overline{N}+1)(\overline{N}+2)}{2}$, be the points belonging to the prediction based neighborhood diction neighborhood, $N(p_0)$. Since a plane represents a first degree predictor (it is capable of reproducing all bivariate polynomials of total degree 1), the order of the dual MRA, $\overline{N} = 2$.The predictor function can be written as

$$z = a_0 + a_1x + a_2y = [1\ x\ y]\theta \quad (15)$$

Where $\theta = [\theta_0 \quad \theta_1 \quad \theta_2]^T$. Let $w = [w_1, w_2, \ldots, w_K]$ be the vector of corresponding weights assigned to the points in the neighborhood. The vector of coefficients, θ, is determined from the points in the neighborhood by solving the system of linear equations,

$$M\,\theta = z$$

Where

$$M = \begin{bmatrix} 1 & x_1 & y_1 \\ M & M & M \\ 1 & x_k & y_k \end{bmatrix}$$

$$z = [z_1, \ldots, z_K]^T$$

The pairs of values (x_k, y_k), $k = 1, \ldots, K$ are the coordinates of the $\overline{N}$ points $p_1, \ldots, p_K$ belonging to the prediction neighborhood with values $z_1, \ldots, z_K$. The least-squares solution for θ is obtained as

$$\theta = M^* z$$

Where M^* is the Moore-Penrose inverse of the matrix M (the Moore-Penrose inverse is unique and exists for all matrices). If the points in the neighborhood are distinct and if all the points do not lie on a straight line, $M^T M$ is non-singular. Then, $M^* = (M^T M)^{-1} M^T$. The prediction weights, w, and the predicted value, $\overline{z_0}$, at point $p_0(x_0, y_0)$ are given by:

$$w = [1\ x_0\ y_0]\ M^*$$
$$z_0 = wz$$

The 1-ring neighborhood with flaps is not considered as a prediction neighborhood for the following reason: the sub-pixel displacement assumption (which is valid and important in multi-frame superresolution) usually results in a grid in which the flap points tend to be nearly collinear with some of the 1-ring neighborhood points. This then increases the computational complexity in determining M^* since $(M^TM)^{-1}M^T$ cannot always be employed due to the possibility of instability of the procedure. In such cases the Moore-Penrose inverse can be computed using the singular value decomposition (SVD) or the QR decomposition. All higher neighborhoods like the 2-ring neighborhood contain the 1-ring neighborhood with flaps as a subset and hence cause the same problem. As mentioned previously, the update step is necessary to ensure that a certain number of moments of the original signal are preserved in the approximations that are successively generated. In the generic 2-D setting, the update operator is implemented based on the area of support of the scaling function as defined in [12]. For any given s_j, the forward wavelet transform or analysis is given by

$$s_{j-1} = \bar{\beta}_j^* s_j \qquad d_{j-1} = \bar{\gamma}_j^* s_j \tag{16}$$

and for any operator U_j,

$$\bar{\beta}_j = \bar{\beta}_j^{(0)} + \bar{\gamma}_j^{(0)} U_j^* \qquad \bar{\gamma}_j = \bar{\gamma}_j^{(0)} \tag{17}$$

From equations (16) and (17)

$$s_{j,N(s_{j,0})} = \bar{\beta}_{j+1}^* s_{j+1}$$

Using Equation (17)

$$s_{j,N(s_{j,0})} = \bar{\beta}_{j+1}^{(0)*} s_{j+1} + U_{j+1} \bar{\gamma}_{j+1}^{(0)*} s_{j+1}$$

And from equations (13) and (14)

$$s_{j,N(s_{j,0})} = s_{j+1,N(s_{j+1,0})} + U_{j+1} d_{j,0} \tag{18}$$

The new lifted dual scaling functions can be obtained using the refinement relation and the prediction equations as

$$\bar{\Psi}_{j,N(s_{j,0})} = \bar{\Psi}_{j+1,N(s_{j+1,0})} + \varpi_{j+1,0} w \tag{19}$$

Where w is the vector of prediction weights employed in the computation of the detail coefficient in Equation (14). Integrating the above expression considering every point $k \in_j N(s_{j+1},0)$,

$$A_{j,k} = A_{j+1,k} + w_k A_{j+1,0} \tag{20}$$

Where $A_{j,k}$ represents the area associated with the support of the scaling function $\varpi_{j,k}$.

For the wavelet,

$$\bar{\xi}_{j,0} = \varpi_{j+1,0} - \bar{\Psi}_{j+1} \bar{\beta}_j U_j$$
$$= \varpi_{j+1,0} - \sum_{k \in N(s_{j+1,0})} \varpi_{j,k} u_{j,k} \tag{21}$$

Stability of the wavelet transform requires that

$$\iint \bar{\xi}_{j,0} = 0 \tag{22}$$

That is, the wavelet should have at least one vanishing moment. This then yields the constraint

$$\iint \varpi_{j+1,0} = \sum_{k \in N(s_{j+1,0})} u_{j,k} \iint \varpi_{j,k} \tag{23}$$

$$A_{j+1,0} = \sum_{k \in N(s_{j+1,0})} A_{j,k} u_{j,k} \tag{24}$$

Since the update values affect the primal wavelet functions, it is desirable to keep them to small magnitudes (otherwise, the wavelet will be very close to the space spanned by the scaling functions at a coarser level leading to instability) [12]. Thus, a solution which satisfies the constraint and is of minimum norm is beneficial. For the constraint given in Equation (24), the minimum norm solution is

$$u_{j,k} = \frac{A_{j,k} A_{j+1,0}}{\sum_{l \in N(s_{j+1,0})} A_l^2} \tag{24}$$

ALGORITHM

An algorithmic description of the process for obtaining a super resolved image from an arbitrarily irregular sampling lattice that results from the registration (using the projective camera motion model) of a set of LR images based on SGWs and the lifting technique (Sweldens, 1998) is presented in this section. The algorithm presented represents a new and seemingly natural approach to superresolution. In addition, simultaneous noise filtering by thresholding of wavelet coefficients is implemented.

Let f_l, l = 1, 2,…, r,…,L represent the LR frames, where f_r denotes the reference LR frame. The coordinate system is defined with respect to f_r. Let $\{p_t(x_t, y_t)\}$ denote

the set of registered pixels obtained using a preselected subset, L_p, of the available degraded LR frames. Let $f_{hr}[k, \ell]$ denote the desired super resolved image which exists on a regular HR grid, the coordinates of which are defined by the rows of a matrix M. The order, $\hat{N}$ of subdivision is determined by the bivariate polynomial of total degree ($\hat{N}$ –1) used for prediction and can be shown [13] to correspond to the number of vanishing moments of the primal or synthesis wavelet. N, the number of vanishing moments of the dual or analysis wavelet $\hat{\psi}$, is chosen in the update step. A closed form expression cannot be given for the dual and primal wavelets (unlike for some FGWs like B-splines) since, in the general second generation setting, wavelets are custom-built to fit the given samples, and hence are arbitrary. The steps of the algorithm are listed below:

1. If the LR frames are not registered, obtain the registered set of points $\{p_t(x_t, y_t)\}$ using the known Registration parameters in the coordinate system R × R defined with respect to f_r. The grid (sampling lattice) so obtained is an irregularly sampled grid (sampling lattice).
2. Define the required HR grid (sampling lattice) in the coordinate system defined above, that is, determine the matrix M. Split M into two sets of points: one set, M_u, is comprised of points whose values are to be updated and retained in the subsequent steps of the algorithm, and another set, M_p, which is to be predicted and eliminated from the coarse representation developed below.
3. For each point in the set M_p, say $f_{hr}[k_0, \ell_0]$:

• Determine the closest point, say $p_0(x_0, y_0)$ from the set $\{p_t(x_t, y_t)\}$ and also its 1-ring neighborhood (or whichever prediction neighborhood is being employed), $N(p_0)$.
• Compute the prediction at $p_0(x_0, y_0)$ by employing a predictor function (such as the least squares plane predictor) using points in $N(p_0)$. It should be noted that boundary points are handled differently, as in (Wang and Bovik, 2002). Subsequently, replace the scaling function coefficient at $p_0(x_0, y_0)$ by the computed detail coefficient which is the error in prediction.
• Determine the area, A0, corresponding to the support of the scaling function at $p_0(x_0, y_0)$, as given in (Wang and Bovik, 2002).
• Coarsen the grid by deleting the point $p_0(x_0, y_0)$ from further consideration.
• Compute areas, A_k, k = 1, . . . ,K, corresponding to the points belonging to the prediction neighborhood.
• Update the scaling function coefficients at points belonging to $N(p_0)$, using a minimum norm update operator.

4. A second generation 2-D surface wavelet has now been defined locally around the point $f_{hr}[k_0, \ell_0]$ on the irregularly sampled registered grid. Compute the detail coefficient at $f_{hr}[k_0, \ell_0]$ by resampling the wavelet surface.
5. To achieve noise reduction, the wavelet/detail coefficients computed are subjected to thresholding.
6. The inverse lifting procedure is now applied on the HR grid to obtain the super resolved image, fhr.

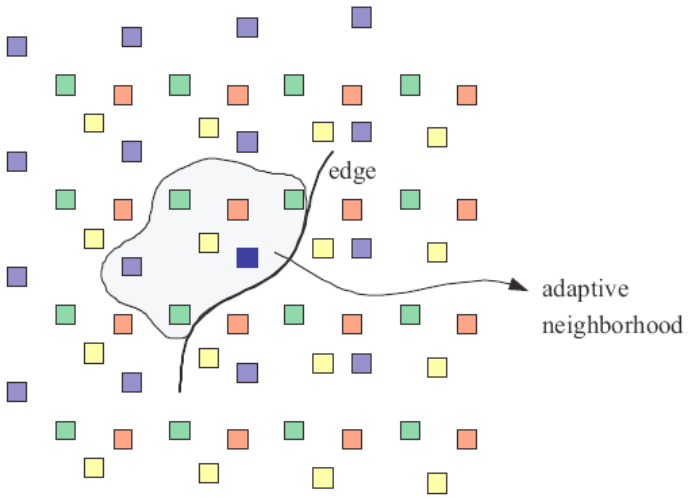

Figure 11. Edge sensitive adaptive neighborhood of a point.

SIMULATION RESULTS

This section presents comparative results which highlight the performance of the generic 2-D SGWSR algorithms. The LR frames used in the simulation (of size 40 × 40 pixels) were generated using an 80×80 image by down-sampling and low-pass filtering. Further, the LR frames are all displaced with respect to each other, but unlike the results presented in Section 4 (in which the displacements were restricted to only translations), the displacements follow the more general projective camera motion model. The LR frames were also corrupted by AWGN at the input. The simulation result shown in Figure 8 employed 6 LR frames and a resolution improvement factor of 2 in each dimension were achieved. It is noted that the use of higher number of good quality LR frames (which can be determined by the preprocessing steps) can not only lead to higher resolution factors, but also to possibly improved noise reduction. A sample LR frame is shown in Figure 12(a) and the original image is shown in Figure 12(b). The SGWSR reconstructions using hard and soft thresholding are given in Figures 12(g) and 12(h) respectively. For comparison, four other HR reconstructtions based on surface approximation and interpolations are given in Figures 12(c)-12(f). It can be observed from Figures 12(c) and 12(d) that direct interpolation (bilinear and bicubic, respectively) of a single LR frame gives, as intuitively expected, the worst visual quality. The outputs of the DTHR methods are better than direct interpolation, but noisy due to the lack of simultaneous noise filtering ability.

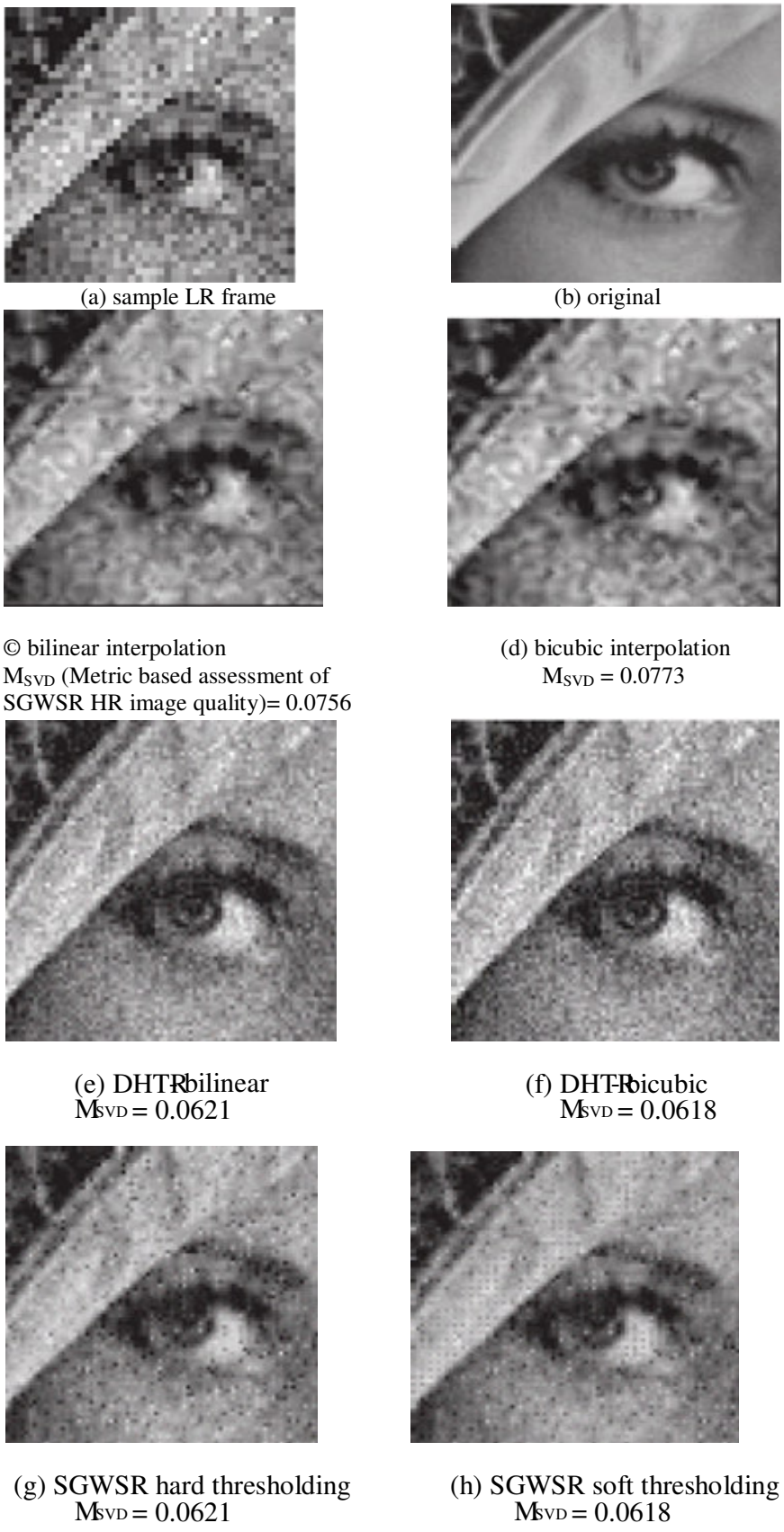

(a) sample LR frame

(b) original

© bilinear interpolation
M_{SVD} (Metric based assessment of SGWSR HR image quality)= 0.0756

(d) bicubic interpolation
M_{SVD} = 0.0773

(e) DHT-Rbilinear
M_{SVD} = 0.0621

(f) DHT-Rbicubic
M_{SVD} = 0.0618

(g) SGWSR hard thresholding
M_{SVD} = 0.0621

(h) SGWSR soft thresholding
M_{SVD} = 0.0618

Figure 12. SGWSR using generic 2-Doperators lenna.

Conclusions

A framework for achieving image sequence superresolution simultaneously with noise filtering has been developped based on SGWs coupled with wavelet coefficient thresholding. The main advantages of the developed procedures are the adaptation to non-uniform sampling lattices, the absence of a priori assumptions on boundary conditions, independence from proper choice of mother wavelets and scaling functions, and the speed of implementation provided by the lifting technique. These advantages coupled with the improved performance in terms of visual quality of the reconstructed HR images make SGWSR algorithms potentially natural and suitable choices for multimedia applications.

REFERENCE

Bose NK, Chappalli MB (2004). A second generation wavelet framework forsuper-resolution with noise filtering. Int. J. Imaging Syst. Technol. Special Issue: High-Resolution Image Reconstruction I. 14(2): 84–89.

Bose NK, Lertrattanpanich S, Chappalli MB (2004). Super-resolution with second generation wavelets. Signal Processing: Image Communication 19(5): 387–391.

Donoho DL (1995). Denoising by soft thresholding. IEEE Transactions on Information Theory. 41(3): 613-627.

El-sayed Waheed M, Mohammed OA (2006). Generalized Gaussian Model for Multi Channel Image Deconvolution 10(3): 127-133.

Lertrattanapanich S, Bose NK (2002). High resolution image formation from low resolution frames using Delaunay triangulation. IEEE Trans. Image Process 2(11): 1427-1441.

Moayeri N, Konstantinides K (1996). An algorithem for blind restoration of blurred and noisy images" Technical Report: HPL-96-102, http://www.hpl.hp.com/techreports/96/HPL-96-102.pdf, Hewlett-Packard Laboratories.

Okabe A, Boots B, Sugihara K (1992). Spatial Tessellations: Concepts and Applications of Voronoi Diagrams, John Wiley & Sons.

Starck JL, Candes EJ, Donoho DL (2002). The curvelet transform for image denoising. IEEE Transactions on Image Processing. 11(6): 670–684.

Sweldens W (1998). The lifting scheme: A construction of second generation wavelets. SIAM J. Math. Anal. 29(2): 511–546.

Vanraes E, Jansen M, Bultheel A (2002). Stabilised wavelet transforms for nonequispaced data smoothing. Signal Processing. 82(12): 1979–1990.

Wang Z, Bovik AC (2002). A universal image quality index. IEEE Signal Process Lett. 9(3): 81–84.

Zayed ASEME, El-sayed Waheed M, Badawy AM, Mohammed OA (2006). Blind Source Recovery Using an Adaptive Generalized Gamma Score Function. Georgian Electron. Sci. J.: Comput. Sci. Telecomm. 9(2): 80-89.